



# Mechanical Properties of Plasma-Sprayed $\text{ZrO}_2$ -8 wt% $\text{Y}_2\text{O}_3$ Thermal Barrier Coatings

Sung R. Choi  
Ohio Aerospace Institute, Brook Park, Ohio

Dongming Zhu  
U.S. Army Research Laboratory, Glenn Research Center, Cleveland, Ohio

Robert A. Miller  
Glenn Research Center, Cleveland, Ohio

## The NASA STI Program Office . . . in Profile

Since its founding, NASA has been dedicated to the advancement of aeronautics and space science. The NASA Scientific and Technical Information (STI) Program Office plays a key part in helping NASA maintain this important role.

The NASA STI Program Office is operated by Langley Research Center, the Lead Center for NASA's scientific and technical information. The NASA STI Program Office provides access to the NASA STI Database, the largest collection of aeronautical and space science STI in the world. The Program Office is also NASA's institutional mechanism for disseminating the results of its research and development activities. These results are published by NASA in the NASA STI Report Series, which includes the following report types:

- **TECHNICAL PUBLICATION.** Reports of completed research or a major significant phase of research that present the results of NASA programs and include extensive data or theoretical analysis. Includes compilations of significant scientific and technical data and information deemed to be of continuing reference value. NASA's counterpart of peer-reviewed formal professional papers but has less stringent limitations on manuscript length and extent of graphic presentations.
- **TECHNICAL MEMORANDUM.** Scientific and technical findings that are preliminary or of specialized interest, e.g., quick release reports, working papers, and bibliographies that contain minimal annotation. Does not contain extensive analysis.
- **CONTRACTOR REPORT.** Scientific and technical findings by NASA-sponsored contractors and grantees.

- **CONFERENCE PUBLICATION.** Collected papers from scientific and technical conferences, symposia, seminars, or other meetings sponsored or cosponsored by NASA.
- **SPECIAL PUBLICATION.** Scientific, technical, or historical information from NASA programs, projects, and missions, often concerned with subjects having substantial public interest.
- **TECHNICAL TRANSLATION.** English-language translations of foreign scientific and technical material pertinent to NASA's mission.

Specialized services that complement the STI Program Office's diverse offerings include creating custom thesauri, building customized databases, organizing and publishing research results . . . even providing videos.

For more information about the NASA STI Program Office, see the following:

- Access the NASA STI Program Home Page at <http://www.sti.nasa.gov>
- E-mail your question via the Internet to [help@sti.nasa.gov](mailto:help@sti.nasa.gov)
- Fax your question to the NASA Access Help Desk at 301-621-0134
- Telephone the NASA Access Help Desk at 301-621-0390
- Write to:  
NASA Access Help Desk  
NASA Center for Aerospace Information  
7121 Standard Drive  
Hanover, MD 21076



# Mechanical Properties of Plasma-Sprayed $\text{ZrO}_2$ -8 wt% $\text{Y}_2\text{O}_3$ Thermal Barrier Coatings

Sung R. Choi  
Ohio Aerospace Institute, Brook Park, Ohio

Dongming Zhu  
U.S. Army Research Laboratory, Glenn Research Center, Cleveland, Ohio

Robert A. Miller  
Glenn Research Center, Cleveland, Ohio

National Aeronautics and  
Space Administration

Glenn Research Center

## Acknowledgments

The authors are grateful to both Ralph Pawlik for experimental work and George Leissler for processing TBC billets. This work was supported by the Ultra-Efficient Engine Technology (UEET) Program, NASA Glenn Research Center, Cleveland, Ohio.

This report is a formal draft or working paper, intended to solicit comments and ideas from a technical peer group.

Trade names or manufacturers' names are used in this report for identification only. This usage does not constitute an official endorsement, either expressed or implied, by the National Aeronautics and Space Administration.

Available from

NASA Center for Aerospace Information  
7121 Standard Drive  
Hanover, MD 21076

National Technical Information Service  
5285 Port Royal Road  
Springfield, VA 22100

Available electronically at <http://gltrs.grc.nasa.gov>

# **Mechanical Properties of Plasma-Sprayed $\text{ZrO}_2$ -8 wt% $\text{Y}_2\text{O}_3$ Thermal Barrier Coatings**

Sung R. Choi  
Ohio Aerospace Institute  
Brook Park, Ohio 44142

Dongming Zhu  
U.S. Army Research Laboratory  
National Aeronautics and Space Administration  
Glenn Research Center  
Cleveland, Ohio 44135

Robert A. Miller  
National Aeronautics and Space Administration  
Glenn Research Center  
Cleveland, Ohio 44135

## **Summary**

Mechanical behavior of freestanding, plasma-sprayed  $\text{ZrO}_2$ -8 wt%  $\text{Y}_2\text{O}_3$  thermal barrier coatings, including strength, fracture toughness, fatigue, constitutive relation, elastic modulus, and directionality, has been determined under various loading-specimen configurations. This report presents and describes a summary of mechanical properties of the plasma-sprayed coating material to provide them as a design database.

## **Introduction**

Thermal barrier coatings (TBCs) have attracted ever-increasing attention for advanced gas turbine and diesel engine applications because of their ability to provide thermal insulation to engine components (refs. 1 to 3). The merits of using ceramic TBCs are well recognized and include a potential increase in engine operating temperature with reduced cooling requirements, resulting in significant improvements in thermal efficiency, performance, and reliability. Plasma-sprayed zirconia-based ceramics are one of the most important coating materials because of their low thermal conductivity, relatively high thermal expansivity, and unique microstructure as a result of the plasma spraying process. However, the durability of TBCs under severe thermal and mechanical loading conditions encountered in heat engines remains one of the major problems. As a result, the development of TBCs requires better understanding of both mechanical and thermal behavior of the coating materials to ensure life and reliability of the engine components.

During the past one to two decades, various plasma-sprayed thermal barrier coating systems have been developed and characterized to determine their mechanical properties such as strength, creep, deformation, elastic modulus, fatigue, and interfacial toughness at ambient and/or elevated temperatures (refs. 4 to 23). These attempts have been made using either freestanding TBCs or TBC-substrate systems. However, few studies have been done to present a multitude of mechanical properties of any given TBC in a single place from which the properties can be conveniently used as a design database.

Mechanical and thermal properties of plasma-sprayed  $\text{ZrO}_2$ -8 wt%  $\text{Y}_2\text{O}_3$  TBCs have been evaluated under various test conditions at the NASA Glenn. Mechanical properties of freestanding, as-sprayed

TBCs are summarized in this report as simply as possible to provide them as a design database. The mechanical properties include strength, fracture toughness, fatigue (slow crack growth), constitutive relation (deformation), elastic modulus, and Poisson's response, determined under various loading-specimen configurations. TBCs exhibit unique microstructure with microcracking, porosity, and lamellar-like splat morphology, so that they would be expected to reveal some directionality of mechanical properties. The directionality effect has been quantified through fracture toughness and Knoop hardness measurements and is also presented in this report. Some of the properties presented here have appeared elsewhere, and those desiring additional details should see references 24 to 29; the data on strength (in part), elastic modulus, Poisson's response, and directionality are appearing here for the first time. A comparison of mechanical properties with other or similar TBC systems was beyond the scope of this report and thus was not made here; the  $\text{ZrO}_2$ -8 wt%  $\text{Y}_2\text{O}_3$  TBC system alone is studied here.

## Experimental Techniques

Unlike dense ceramics, the stress-strain behavior of as-sprayed TBCs is not linear-elastic. Therefore, applying conventional test methods that are employed for dense materials may not be pertinent, in a rigorous sense, to TBCs. However, since no standardized test methods are currently available for TBCs, most of the experimental techniques used here to determine their mechanical properties were followed in principle in accordance with ASTM test standards that are primarily applied to dense advanced ceramics that are commonly regarded to be isotropic and homogenous.

### Material

The  $\text{ZrO}_2$ -8 wt%  $\text{Y}_2\text{O}_3$  powder (Zircoa, Inc., Solon, OH) with an average particle size of  $60\text{ }\mu\text{m}$ , fabricated by sintering and crushing, was first plasma-sprayed on a graphite substrate measuring 150 by 100 by 6.5 mm to a thickness of about 6 mm, using a Sulzer-Metco ATC-1 plasma coating system (Sulzer Metco, Inc., Westbury, NY) with an industrial robot. The plasma-spray conditions can be found elsewhere (ref. 30). Freestanding, as-sprayed ceramic billets were then obtained by burning away the graphite substrate at  $680\text{ }^\circ\text{C}$  in air for 24 h. The billets were machined into test specimen configurations such as cylindrical rods, flexure beams, or disks, depending on test matrix. Figure 1 shows a typical layered structure, a polished surface, and a fracture surface, showing the microstructure of as-processed coatings, in which a large number of microcracks and pores are characterized in conjunction with a splat (platelet) structure. It has been found that the coatings primarily consist of the tetragonal  $t'$  phase (ref. 8) and have a density of  $5.147 \pm 0.020\text{ g/cm}^3$  with a porosity of about 10 percent.

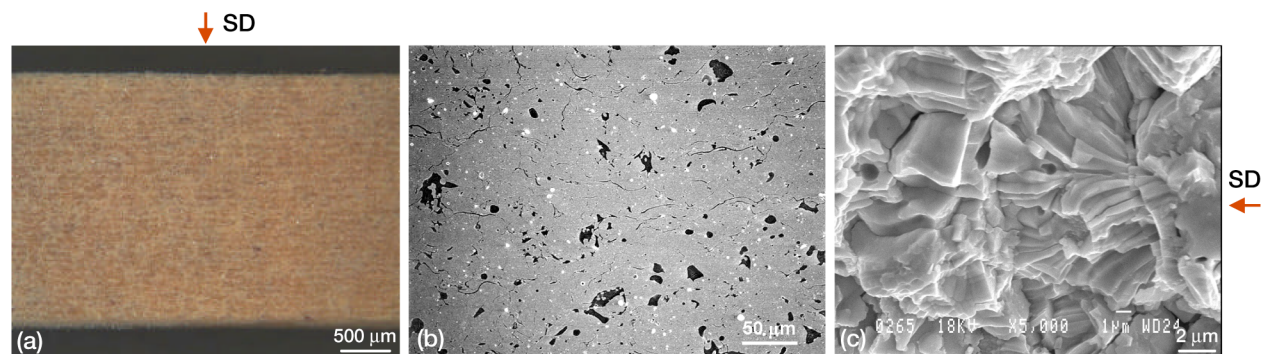


Figure 1.—Typical microstructures of plasma-sprayed  $\text{ZrO}_2$ -8 wt%  $\text{Y}_2\text{O}_3$  thermal barrier coatings. “SD” indicates plasma-spray direction. (a) Side view of flexure specimen showing lamellae (layers). (b) Polished top surface. (c) Fracture surface.

## Strength

The five different loading-specimen configurations used in strength testing at ambient temperature (25 °C) were uniaxial tension, transthickness tension, uniaxial compression, four-point uniaxial flexure, and ring-on-ring biaxial flexure. Schematics of test specimens and direction of applied load with respect to plasma-spray direction are shown in figure 2. Dimensions of test specimens and corresponding test methods (ASTM C 1273, C 1468, C 1424, and C 1161 in refs. 31 to 34, respectively) are shown in table I. Note that in certain cases some variations in test specimens' dimensions from the specifications of related ASTM test standards were inevitable, due to the limited size of the coating material. The final finish of test specimens was achieved using #500 diamond grinding wheel. For test specimens with a round section, a combination of surface and cylindrical grinding was used. Testing was performed at a test rate of 0.5 mm/min using an electromechanical test frame (Model 8562, Instron Corporation, Canton, MA). The magnitude of strength was found almost independent whether the top surface was placed in tension or the bottom surface previously in contact with the graphite substrate was placed in tension, as determined with four-point flexure bars.

## Fracture Toughness

The method used to determine fracture toughness in modes I and II at 25, 800, and 1316 °C was the single edge V-notched beam (SEVNB) technique (ref. 35). Sharp V notches in which final notch depth and root radius were 2.0 mm and 20 to 50  $\mu\text{m}$ , respectively, were introduced in flexure test specimens (3 by 4 (depth) by 25 to 50 mm). Through-the-thickness sharp notches thus prepared were aligned parallel with respect to the plasma spraying direction. Other methods used to generate sharp cracks to estimate

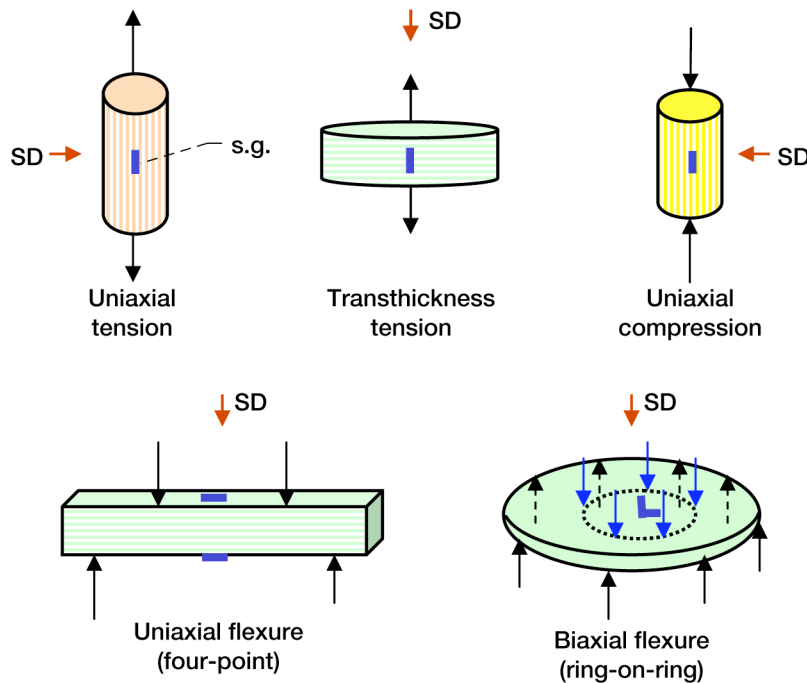


Figure 2.—Five different loading-specimen configurations used in strength testing of plasma-sprayed  $\text{ZrO}_2$ -8 wt%  $\text{Y}_2\text{O}_3$  thermal barrier coatings. “SD” indicates plasma-spray direction. Strain gages (s.g.) attached are also indicated: note that biaxial strain gage was placed in tension side of biaxial disk.

TABLE I.—RESULTS OF STRENGTH TESTING FOR PLASMA-SPRAYED  $\text{ZrO}_2$ -8wt%  $\text{Y}_2\text{O}_3$  THERMAL BARRIER COATINGS IN FIVE DIFFERENT LOADING-SPECIMEN CONFIGURATIONS AT AMBIENT TEMPERATURE

Type of testing	Test method	Specimen dimensions, <sup>a</sup> mm	Number of test specimens	Direction of fracture <sup>b</sup>	Average strength, <sup>c</sup> MPa	Weibull modulus, <i>m</i>
Uniaxial tension	ASTM C 1273	5×15 (diam×L)	10	P	15(1)	7
Transthickness tension	ASTM C 1468	15×3 (diam×T)	10	N	11(1)	13
Uniaxial compression	ASTM C 1424	5×10 (diam×L)	10	P/N	300(77)	4
Uniaxial flexure (four-point)	ASTM C 1161	3×4×25 to 50 (H×W×L), 20/40- or 10/20-mm spans	30	P	33(7)	6
Biaxial flexure (ring-on-ring)	-----	25×3 (diam×T) (11/22 mm rings)	10	P	40(4)	12

<sup>a</sup>Diam is diameter; L, length; T, thickness; H, height; W, width.

<sup>b</sup>Direction of fracture with respect to the plasma-spray direction. P is parallel; N, normal.

<sup>c</sup>Numbers in parentheses indicate  $\pm 1.0$  standard deviation.

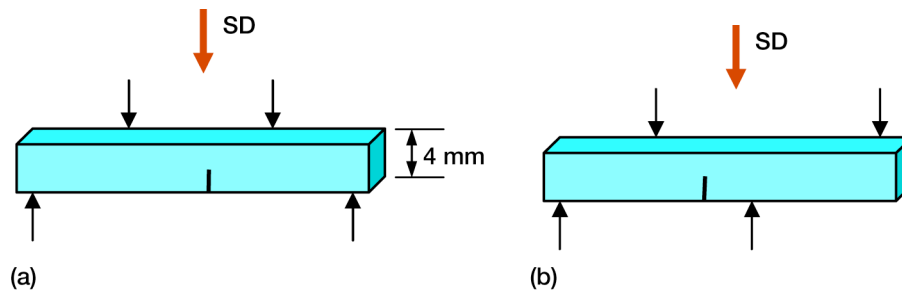


Figure 3.—Test specimen and loading configurations used in fracture toughness testing for plasma-sprayed  $\text{ZrO}_2$ -8 wt%  $\text{Y}_2\text{O}_3$  thermal barrier coatings; “SD” indicates plasma-spray direction. (a) Mode I testing ( $K_{Ic}$ ) in symmetric four-point flexure. (b) Mode II testing ( $K_{IIc}$ ) in asymmetric four-point flexure.

fracture toughness, such as the single edge precracked beam and the surface crack in flexure techniques (ASTM C 1421, ref. 36) by indentation, were not feasible for the coating material, since indentation response was very poor because of the material’s significant porosity and microcracks. Modes I and II fracture toughness  $K_{Ic}$  and  $K_{IIc}$  were determined in symmetric and asymmetric four-point flexure, respectively, as shown in figure 3. Testing was performed in air at a test rate of 0.5 mm/min using the electromechanical test frame. At elevated-temperature testing, each test specimen was heated at a rate of about 20 °C/min and held for 15 min at test temperature for about 15 min prior to testing. Typically, more than four specimens were tested in each mode at a given temperature.

### Fatigue (Slow Crack Growth)

Dynamic fatigue (constant stress rate) testing in accordance with ASTM C 1368 and C 1465 (refs. 37 and 38, respectively) was performed in flexure at 25 and 800 °C in air to evaluate slow-crack-growth behavior of the coating material. The dimensions of test specimens were identical to those used in



uniaxial four-point flexure strength or fracture toughness testing. The number of stress rates was three, 50, 0.05, and 0.0005 MPa/s, and the number of test specimens was five at each stress rate. Cyclic fatigue (cyclic stress) testing was also conducted in tension at 25 °C in air using uniaxial tensile test specimens (see fig. 2) with a stress ratio of  $R = 0.1$  at a frequency of 10 Hz ( $R = \sigma_{\min}/\sigma_{\max}$ , where  $\sigma$  is applied stress). Dynamic and cyclic fatigue testing were conducted using electromechanical (Model 8562) and servohydraulic (Model 8502, Instron, Canton, MA) test frames.

### **Constitutive Relation and Deformation Behavior**

Strain gages were used to determine constitutive relations (stress-strain curves or deformation behavior) for different loading-specimen configurations used in the strength testing (fig. 2). Typically, one test specimen with one strain gage aligned along the principal stress direction was used for each configuration. In ring-on-ring biaxial flexure, a biaxial strain gage was placed at the center of the disk in tension side. Particularly, in four-point flexure loading, two strain gages—one in tension and another in compression—were employed to determine the constitutive relations in both sides of a test specimen.

### **Elastic Modulus and Poisson's Ratio**

Elastic modulus was determined from the slopes of the stress-strain curves obtained from the “constitutive relation” testing. In addition, the impulse excitation technique, ASTM C 1259 (ref. 39), was employed using flexure test specimens (3 by 4 by 50 mm) to determine elastic modulus in both directions at ambient temperature. Direction 1 corresponds to the case that excitation in flexure mode is made on the 4 mm side of a test specimen, while direction 2 is the case when excitation is made on the 3 mm side. Five test specimens were used.

Poisson's ratio was estimated with a uniaxial compression test specimen (fig. 2) by determining both longitudinal and transverse strains via two strain gages that were oriented perpendicular to each other. A test specimen annealed at 1316 °C in air for 500 h was also used for comparison.

### **Directionality**

The effect of direction of the mechanical properties of as-sprayed TBCs was examined using flexure test specimens by determining both mode I fracture toughness and microhardness as a function of material axis, as shown in figure 4. Fracture toughness (see fig. 4(a)) in direction 2 was determined by the SEVNB method, whereas fracture toughness in direction 3 (i.e., the interlamina direction) was determined by the double cantilever beam (DCB) method with a sharp V notch introduced in the midplane of the test specimens. Four to five flexure test specimens were tested for each direction. Fracture toughness in the DCB specimens was calculated based on the formula by Murakami (ref. 40).

Knoop microhardness, in accordance with ASTM C 1326 (ref. 41), was determined with a four-point flexure test specimen (see fig. 4(b)) at both 0° and 90° on its top (perpendicular to plasma-spraying direction) and side (parallel to plasma-spraying direction) surfaces. An indentation load of 9.8 N was used with a total of five indents at each orientation for a given specimen surface.

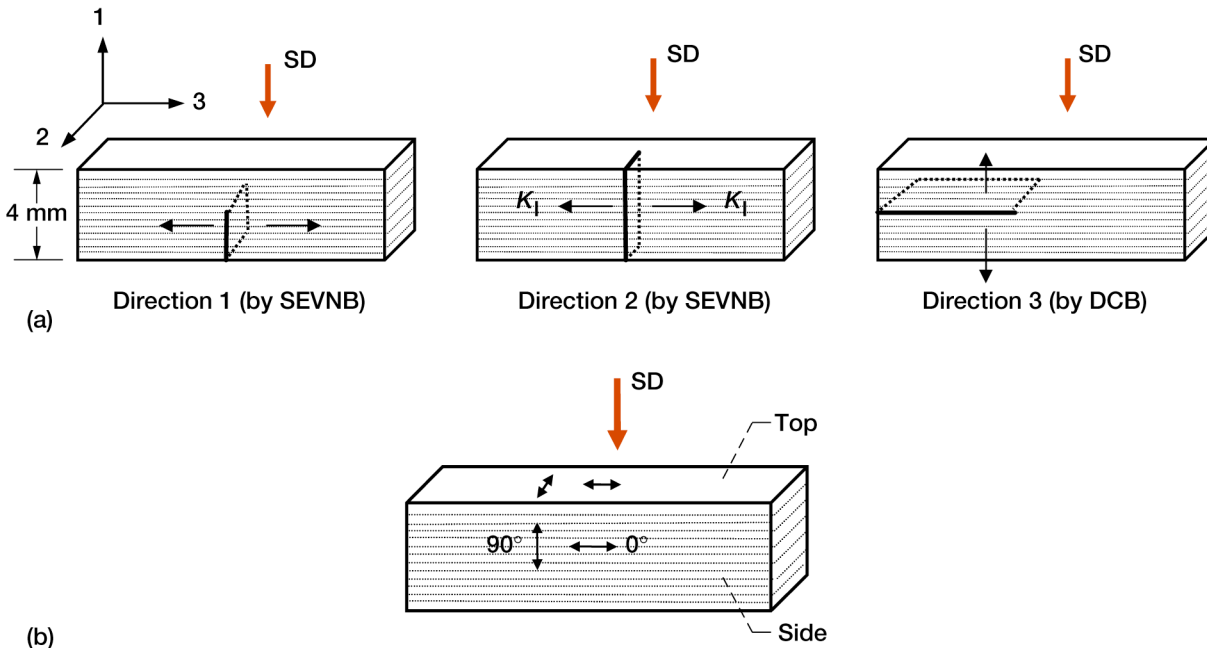


Figure 4.—Schematics to examine directionality effect of as-sprayed  $\text{ZrO}_2$ -8 wt%  $\text{Y}_2\text{O}_3$  thermal barrier coatings. Horizontal lines in test specimens show lamellar-like layers, oriented normal to plasma-spray direction. “SD” indicates plasma-spray direction. (a) Mode I fracture toughness testing in three orientations. (b) Knoop microhardness determined at two different orientations of  $0^\circ$  and  $90^\circ$  at both top and side surfaces.

## Mechanical Properties

### Strength

A summary of strength for five different loading-specimen configurations is shown in table I. Of the five loading-specimen configurations considered, transthickness tensile strength is lowest ( $11 \pm 1$  MPa) but somewhat comparable to uniaxial tensile strength ( $15 \pm 1$  MPa). Ring-on-ring biaxial flexure strength was highest at  $40 \pm 4$  MPa. Uniaxial flexure strength, determined with a total of 30 test specimens, was  $33 \pm 7$  MPa, which is significantly lower than that (270 MPa) of hot-pressed 10 mol% yttria-stabilized zirconia (YSZ) (ref. 42). Uniaxial flexural strength has been observed to be little influenced by vintage, indicating consistency in plasma-spray processing over the years (refs. 24, 25, and 29).

Two-parameter Weibull strength distributions, notwithstanding the insufficient number (which was 10, except for four-point flexure with 30) of test specimens used, were made for comparison and are shown in figure 5. Weibull modulus  $m$  of TBCs ranged from 6 for uniaxial flexure to 13 for transthickness tension, similar to a typical range observed for many dense monolithic ceramics. Effect of specimen size on strength is depicted in figure 6, in which strength was plotted against (a) effective area  $A_{\text{eff}}$  and (b) effective volume  $V_{\text{eff}}$  for various test specimens used. The effective area and effective volume for both uniaxial and biaxial flexure were calculated based on an average value of Weibull modulus,  $m = 10$ . Prediction of strength for each case was made with a reference strength value in uniaxial flexure together with  $m = 10$ , based on the principle of independent action (PIA). No reasonable agreement between the prediction and the data was found for the surface-flaw controlled case, as shown in figure 6(a). However, the trend observed the case of volume flaws was closer to the predicted, as seen in figure 6(b), implying that the common notion of the size effect that is employed to dense brittle materials may be applicable to TBCs at least for volume flaws. In other words, the difference in strength of TBCs

between different specimen geometries would be explained at minimum by the specimen size effect associated with volume flaws. However, the deviation of prediction from the data still indicates that inconsistency in flaw populations was much more predominant in complexly structured TBCs than in relatively homogeneous dense brittle ceramics.

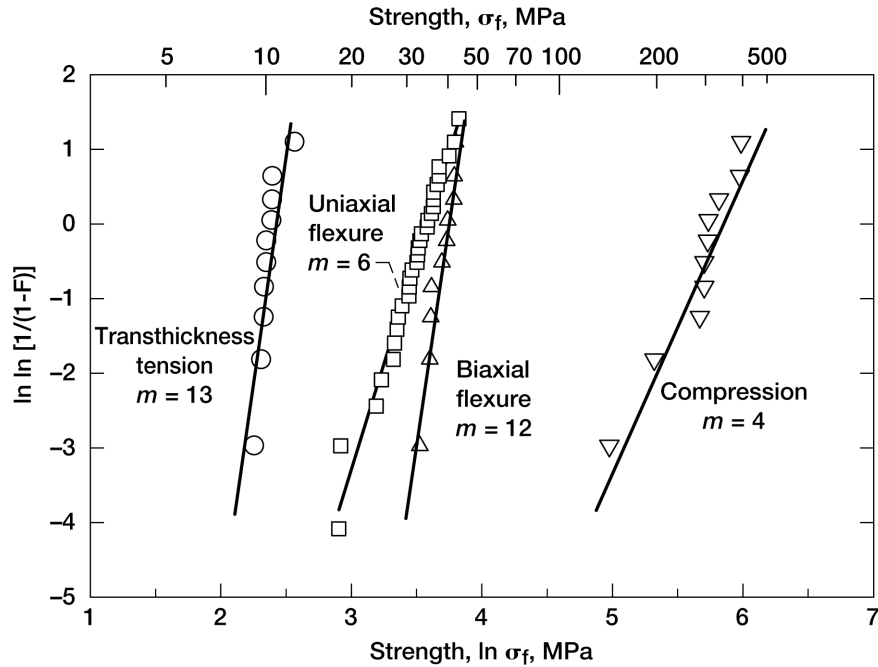


Figure 5.—Weibull strength distributions determined in transthickness tension, uniaxial flexure, biaxial flexure, and compression for plasma-sprayed  $\text{ZrO}_2\text{-8 wt\% Y}_2\text{O}_3$  thermal barrier coatings. “F” indicates failure probability.

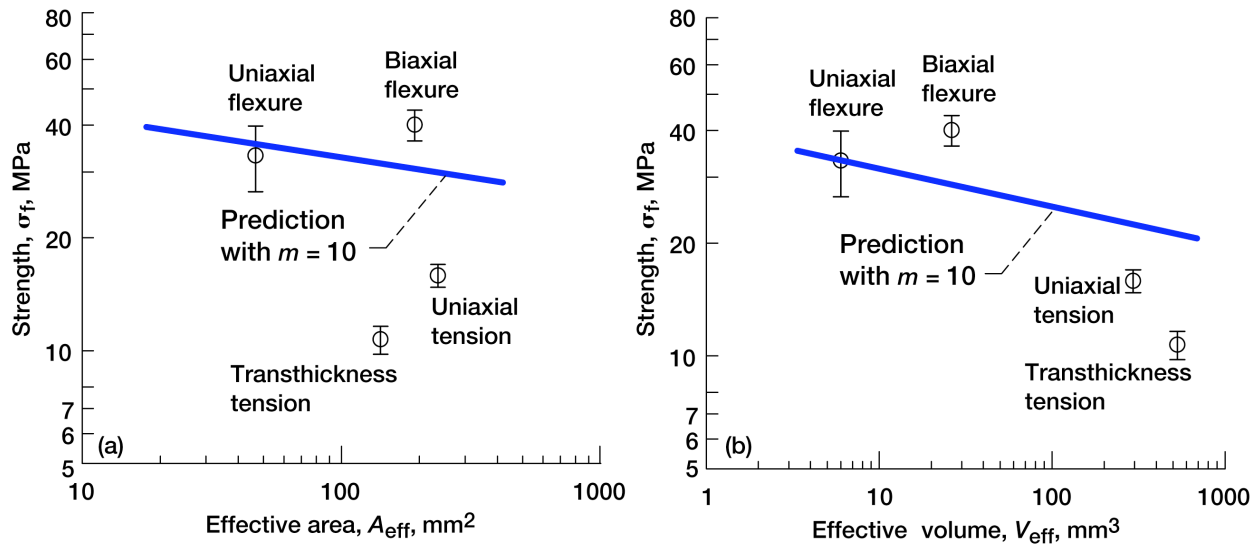


Figure 6.—Plots of strength against (a) effective surface area  $A_{\text{eff}}$  and (b) effective volume  $V_{\text{eff}}$  in uniaxial tension, transthickness tension, uniaxial flexure, and biaxial flexure for plasma-sprayed  $\text{ZrO}_2\text{-8 wt\% Y}_2\text{O}_3$  thermal barrier coatings. Prediction of strength based on principle of independent action (PIA) with Weibull modulus of  $m = 10$  for uniaxial flexure was presented for each case.

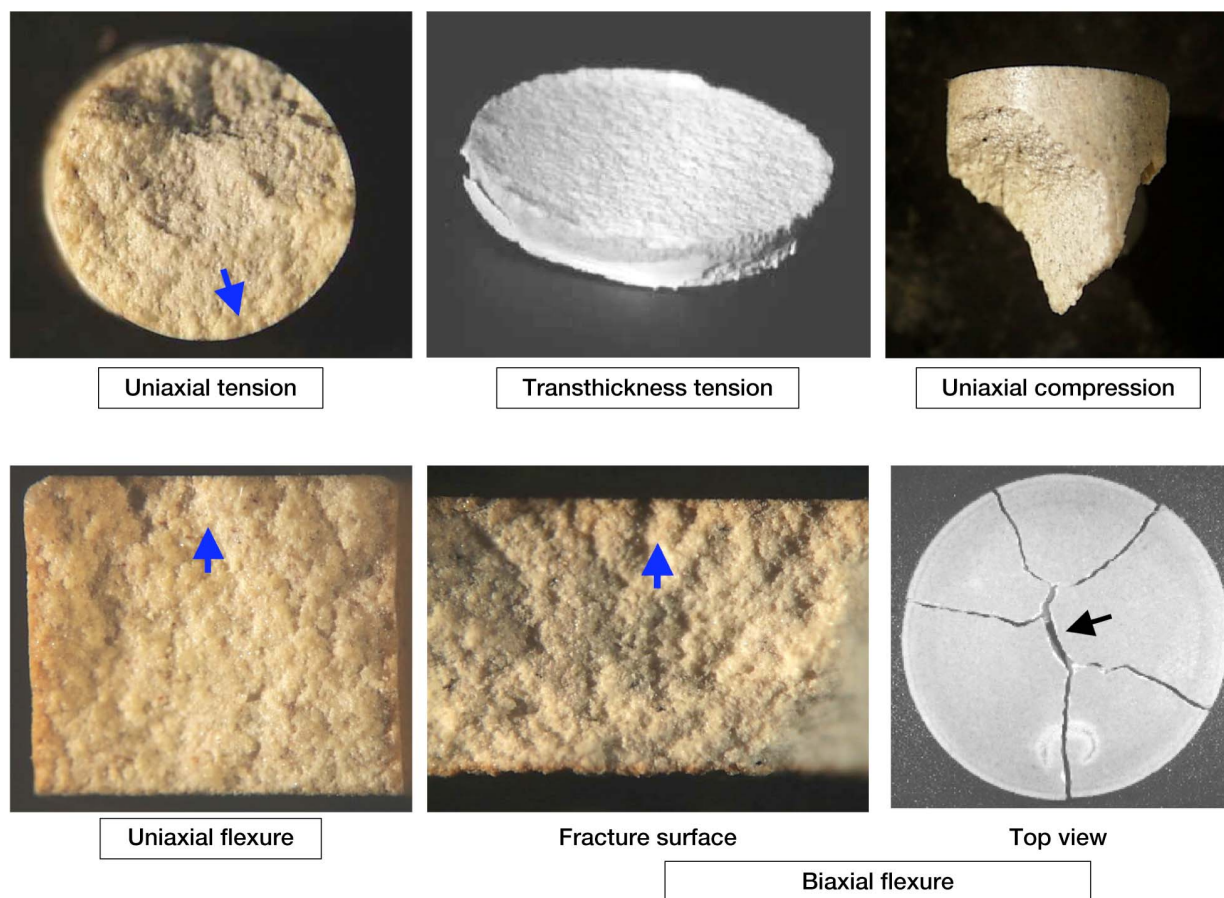


Figure 7.—Modes of fracture and fracture surfaces of tested specimens subjected to different loadings for plasma-sprayed  $\text{ZrO}_2$ -8 wt%  $\text{Y}_2\text{O}_3$  thermal barrier coatings at ambient temperature. Arrows indicate probable fracture origins.

Typical examples of fracture surfaces and fracture modes of various tested specimens are shown in figure 7. Fracture surfaces of TBCs are typified such that exact fracture origins and their nature were hardly identifiable, because of the loosely connected, open structure, which also yielded significantly low strength. Probable fracture origins are indicated with arrows in the figure. For dense brittle materials, the fracture origin can be easily identified from a well-developed region of the fracture mirror, and its nature can be explored in relative simplicity. Hence, unlike dense brittle ceramics, TBCs give rise to an enormous challenge in fractography.

### Fracture Toughness

A summary of modes I and II fracture toughness is presented in figure 8. The values of  $K_{Ic}$  and  $K_{IIc}$  represent the average of four and eight measurements, respectively, at 25 °C and the average of four measurements for each tested at 1316 °C. The values of fracture toughness were  $K_{Ic} = 1.15 \pm 0.07$ ,  $1.03 \pm 0.07$ , and  $0.98 \pm 0.13 \text{ MPa } \sqrt{\text{m}}$  at 25, 800, and 1316 °C, respectively, whereas  $K_{IIc} = 0.73 \pm 0.10$  and  $0.65 \pm 0.04 \text{ MPa } \sqrt{\text{m}}$  at 25 and 1316 °C, respectively. This indicates that fracture toughness in either mode I or mode II remained almost consistent regardless of temperature up to 1316 °C.  $K_{IIc}$  was about 35 percent lower than  $K_{Ic}$ . It has been reported that for some dense ceramics,  $K_{IIc}$  was greater than  $K_{Ic}$ ,

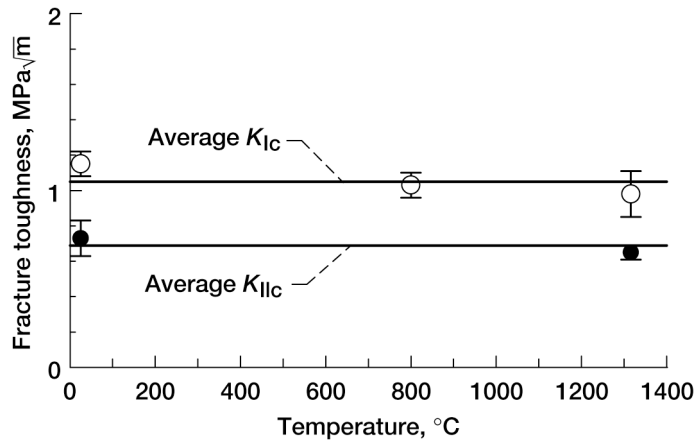


Figure 8.—Fracture toughnesses  $K_{Ic}$  and  $K_{IIc}$  as function of test temperature for plasma-sprayed  $ZrO_2$ -8 wt%  $Y_2O_3$  thermal barrier coatings tested with single edge V-notched beam (SEVNB) technique.

It must be noted that the effect of sintering on fracture toughness during elevated-temperature testing particularly at 1316 °C was found to be negligible based on a sintering study in which fracture toughness increase of the coating material was about 0.12 MPa  $\sqrt{m}/h$  for the first 5-h annealing at 1316 °C in air (ref. 29). This indicates that the fracture toughness increase observed in the present tests at 1316 °C would be about 3 percent. Therefore, care must be exercised in interpreting test results when even higher test temperatures and/or longer test durations are used. This caution applies to any mechanical testing for plasma-sprayed TBCs at elevated temperatures.

### Fatigue (Slow Crack Growth)

Fatigue (slow crack growth) behavior of TBCs at 25 °C in tension and at 800 °C in flexure is shown in figure 9. The coating material exhibited a negligible susceptibility to cyclic fatigue in tension at 25 °C with a significant fatigue parameter  $n > 100$ , as shown in figure 9(a). The fatigue parameter  $n$  is from the conventional power-law type of crack growth, expressed as

$$V = \alpha \left( \frac{K_I}{K_{Ic}} \right)^n$$

where  $V$  is crack velocity,  $\alpha$  is another fatigue parameter, and  $K_I$  is Mode I stress intensity factor. At 800 °C, the coating material did not exhibit any fatigue (i.e.,  $n > 100$ ), but rather a strength increase with decreasing applied test rate, attributed to some minor sintering effect at lower test rates, as shown in figure 9(b). These results indicate that the resistance to fatigue or slow crack growth of as-sprayed TBCs was very significant at both temperatures, implying that slow crack growth under either cyclic tension or monotonic flexure would be hindered by frequent entrapping of a growing crack at the pore- and/or microcrack-rich regions. The significant resistance of TBCs to fatigue was also observed in cyclic tension at ambient temperature by Wesling, Socie, and Beardsley (ref. 48).

presumably attributed to frictional interaction between the two facing crack planes (ref. 43). However, the previous studies on advanced dense ceramics including silicon nitrides, alumina, and zirconia (refs. 44 and 45) showed a different result:  $K_{IIc}$  was almost identical to  $K_{Ic}$ , indicative of an insignificant frictional effect on  $K_{IIc}$  by either coarse-grained or fine-grained ceramics. The coating material, however, did not exhibit similar values in both  $K_{IIc}$  and  $K_{Ic}$  but rather yielded a lower value in  $K_{IIc}$  than in  $K_{Ic}$  at both 25 and 1316 °C. Hot-pressed 10 mol% YSZ showed a value of  $K_{Ic} = 1.7 \text{ MPa } \sqrt{m}$  at 25 °C (ref. 42), consistent with other dense YSZs (with >8 mol% yttria) exhibiting  $K_{Ic} = 1 \text{ to } 2 \text{ MPa } \sqrt{m}$  (refs. 46 and 47).

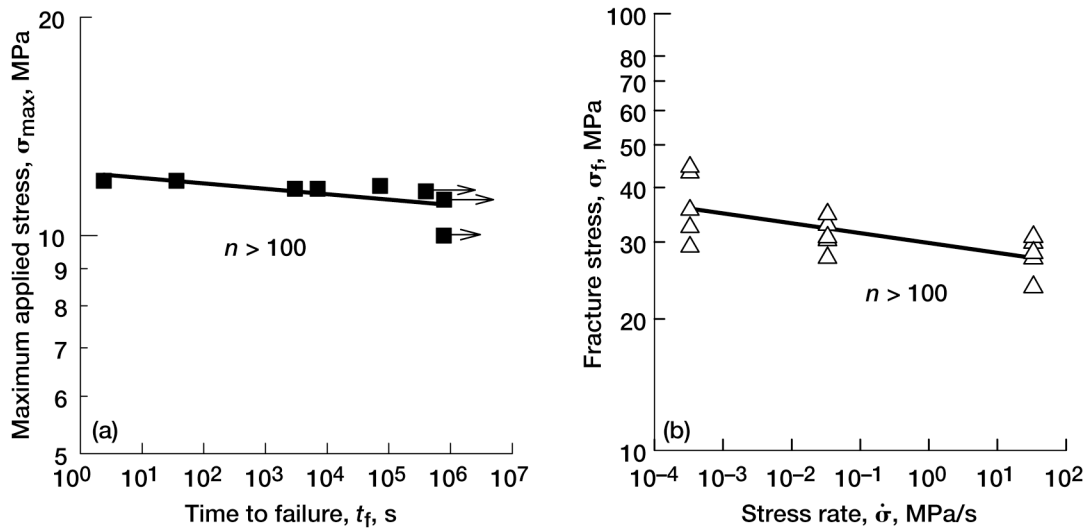


Figure 9.—Results of fatigue (slow crack growth) testing for plasma-sprayed ZrO<sub>2</sub>-8 wt% Y<sub>2</sub>O<sub>3</sub> thermal barrier coatings. (a) Cyclic fatigue (cyclic stress) testing in tension at 25 °C in air. (b) Dynamic fatigue (constant stress rate) testing in flexure at 800 °C in air.

### Constitutive Relation and Deformation Behavior

Figure 10 shows the stress-strain curves in tension, compression, biaxial flexure, and uniaxial flexure. TBCs did not exhibit any idealized linear elasticity in either loading or unloading, resulting in an appreciable hysteresis in one full loading-unloading sequence. A similar nonlinear elastic behavior was also found previously by the authors (unpublished) in sandstone that possesses a TBC-like, loosely connected, open microstructure. Despite their nonlinearity, as-sprayed TBCs revealed almost elastic behavior with little plastic deformation. The nonlinear elastic behavior was independent of loading rate, number of cycles, and type of loading configurations in either tension, compression, or flexure (refs. 24, 26, and 27). The initial stress-strain curves were altered slightly as the number of loading-unloading cycles increased, as seen in figures 10(a) and (c). However, once the number of cycles was beyond 10 or so, the difference in the shape of stress-strain curves remained almost unchanged. This indicates that any notable damage evolution, such as crack propagation, microcracking, and/or mechanical-interlocking loosening, would not have occurred under repeated loading-and-unloading sequences. The stress-strain curve of a uniaxial flexure test specimen exhibited greater stiffness in compression than in tension, evidence of the loosely connected, open microstructure of TBCs. Several sequences of loading and unloading with different levels of compressive stress are shown in figure 11. This figure shows that regardless of applied stress, each loading curve follows the same loading path, whereas the unloading curve follows a unique path from the respective peak stress, eventually returning back to its original starting point.

### Elastic Modulus and Poisson's Ratio

**Elastic modulus.**—Due to significant nonlinear behavior of its stress-strain curves, a single-valued elastic modulus of the coating material cannot be determined. Rather, different values of elastic modulus are evaluated, depending on the type of loading and on the magnitude of applied stress. The most accurate approach, of course, is to use the *tangent modulus* ( $E = d\sigma/d\epsilon$ ) of elasticity, which is the slope of a stress ( $\sigma$ )-strain ( $\epsilon$ ) curve at any point for a given loading or unloading sequence (refs. 22 and 26). With this

approach, an assessment of elastic modulus could be made for a given range of applied stress, consistently from specimen to specimen. However, this approach is not practical—particularly in design, analysis, and lifing, in which single values of elastic modulus are predominantly desirable.

Alternatively, if the variation of slopes in the curves is not significant from the lowest stress to the peak, the slope between these two extreme points, the *secant modulus* of elasticity in a broad sense, could be used as an approximated value of elastic modulus. This alternative approach, applied to tension and compression in each of their loading sequences in figures 10(a) and (b), yielded an elastic modulus of  $E_t \approx 13$  GPa in tension and  $E_c \approx 25$  GPa in compression. The variation of elastic modulus with different levels of applied stress, for example in compression, was negligible with  $E_c \approx 22$  to 25 GPa at applied stresses of 10, 20, 30, and 45 MPa. It is noted that elastic modulus in pure tension,  $E_t = 13$  GPa, is comparable with  $E_t = 16$  GPa in transthickness tension (ref. 26), where the latter was evaluated between applied stresses of 0 to 5 MPa. However, this secant-modulus approach does not account for the hysteresis and would not be appropriate for the unloading sequences. Because of the difference in elastic modulus between tension and compression, a neutral-axis shift should be taken into account in calculating stresses in uniaxial and biaxial flexure. The stresses in both biaxial and uniaxial flexure shown in figures 10(c) and (d), respectively, were calculated based on the linear elastic approach without considering the neutral-axis shift for simplicity. Without considering the neutral-axis shift, the elastic modulus was determined to be  $E = 44$  GPa with Poisson ratio of 0.04 in biaxial flexure (fig. 10(c)), and  $E = 24$  and 30 GPa in tension and compression sides, respectively, in uniaxial flexure (fig. 10(d)).

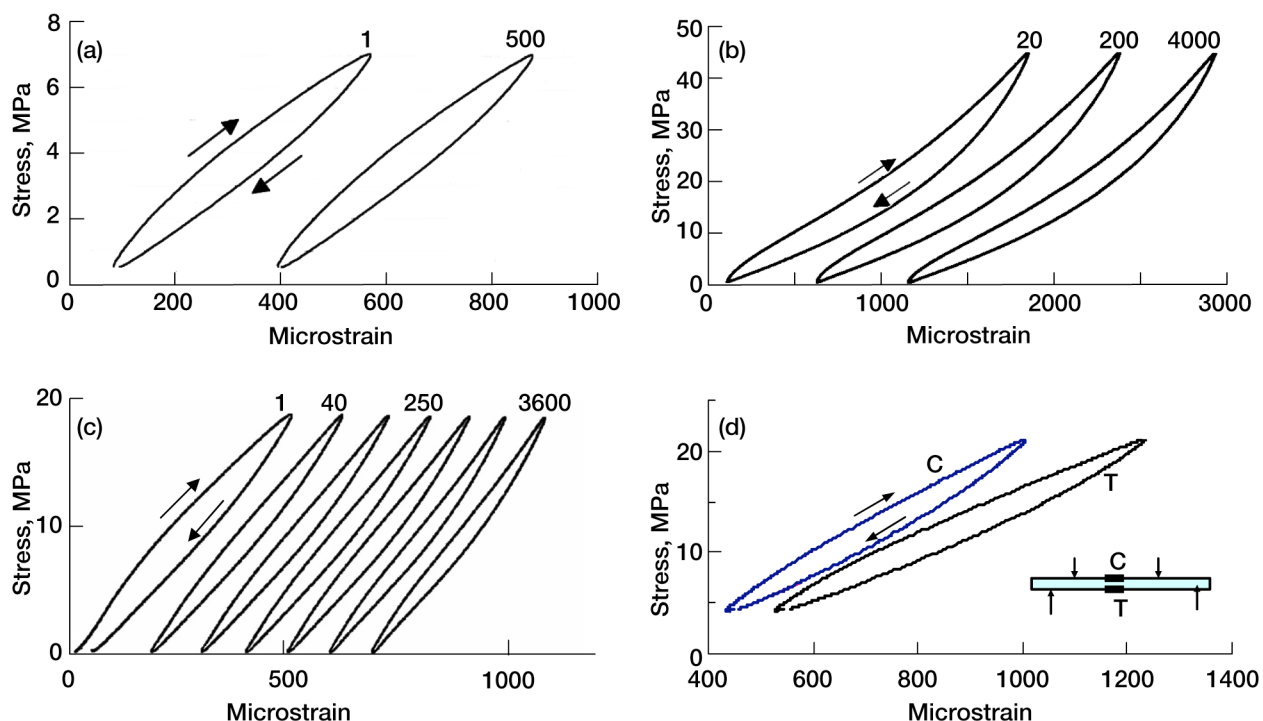


Figure 10.— Stress-strain curves determined for plasma-sprayed  $\text{ZrO}_2$ -8 wt%  $\text{Y}_2\text{O}_3$  thermal barrier coatings. Number of loading-unloading cycles are indicated at top of curves in (a) to (c). (a) Uniaxial tension. (b) Compression. (c) Biaxial flexure. (d) Uniaxial flexure showing responses of tension (T) and compression (C) sides.



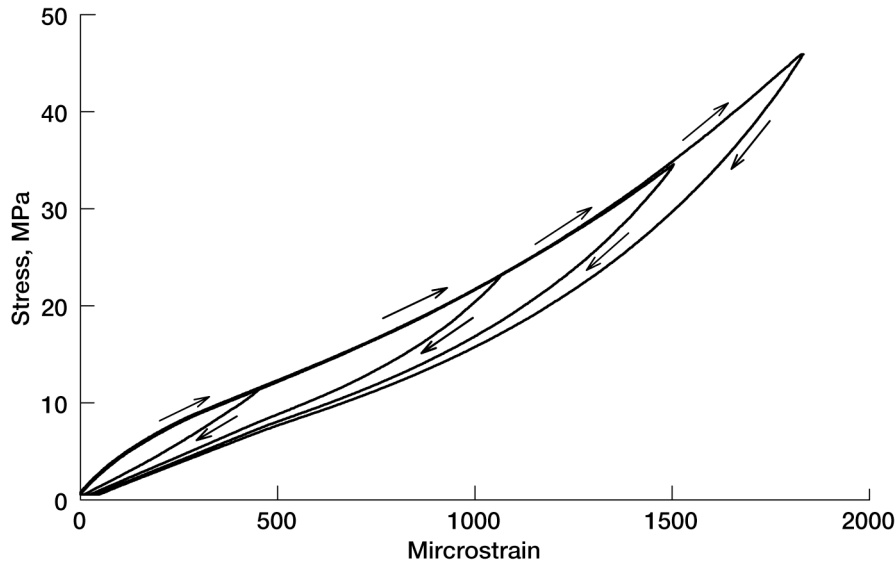


Figure 11.— Stress-strain curve determined in compression using cylindrical rod test specimen of plasma-sprayed  $\text{ZrO}_2$ -8 wt%  $\text{Y}_2\text{O}_3$  thermal barrier coatings with different loading-unloading sequences with different peak stresses.

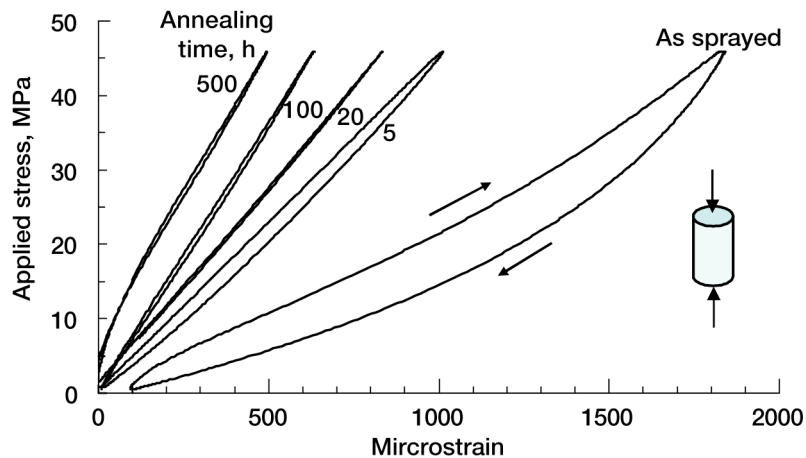


Figure 12.—Stress-strain curves at different annealing times for plasma-sprayed  $\text{ZrO}_2$ -8 wt%  $\text{Y}_2\text{O}_3$  thermal barrier coatings annealed at  $1316^\circ\text{C}$  in air, determined at  $25^\circ\text{C}$  in compression by strain gaging.

The situation that elastic modulus varies with applied stress could be changed when TBCs are annealed at elevated temperatures, so that gradually increasing linearity develops with increasing annealing time, as shown in figure 12 (ref. 29). The stress-strain curves in the figure were obtained in compression at  $25^\circ\text{C}$  after annealing cylindrical compression test specimens at  $1316^\circ\text{C}$  in air. This change in constitutive relation was attributed to sintering in which the coating material was converted from a loosely connected to a more closely connected microstructure. The values of elastic modulus were  $E \approx 45, 55, 75$ , and  $77$  GPa, respectively, for 5, 20, 100, and 500 h annealing time, while the as-sprayed value was  $E \approx 25$  GPa, as previously mentioned. In view of this systematic change in constitutive relation,



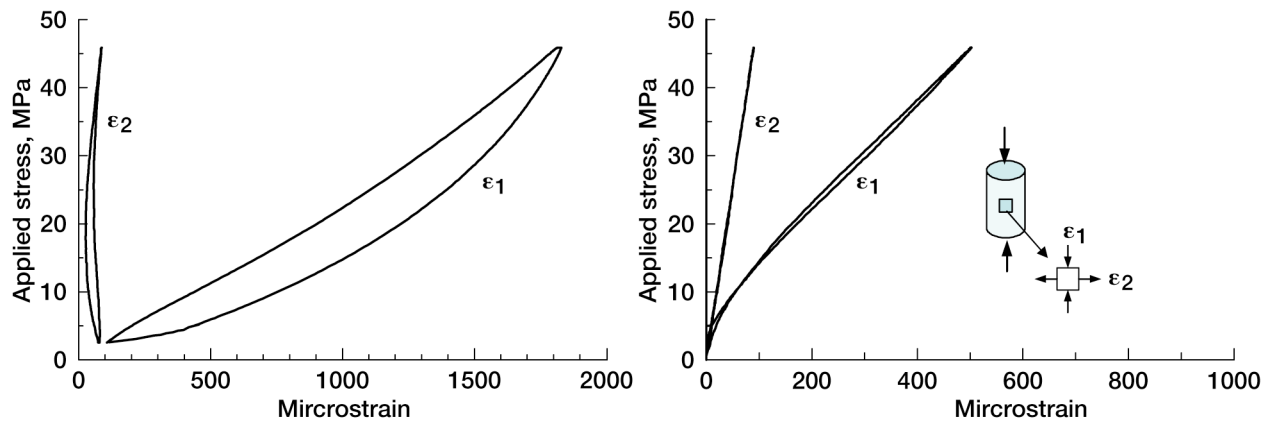


Figure 13.—Stress-strain curves for compression in both longitudinal ( $\epsilon_1$ ) and transverse ( $\epsilon_2$ ) directions of plasma-sprayed  $\text{ZrO}_2$ -8 wt%  $\text{Y}_2\text{O}_3$  thermal barrier coatings. (a) As-sprayed condition. (b) Annealed at  $1316^\circ\text{C}$  for 500 h in air.

it would be reasonable to use the two extreme points of a curve, as a first order of approximation, in order to estimate an approximated value of elastic modulus of as-sprayed TBCs. The effect of sintering on various mechanical properties of TBCs has been determined in detail in a previous study (ref. 29).

The values of elastic modulus determined by the impulse excitation technique were  $E = 36 \pm 2$  and  $39 \pm 2$  GPa, respectively, for directions 1 and 2 (see fig. 4(a)). Note the insignificant difference between the values in the two directions. The values of elastic modulus determined by impulse excitation were greater than those determined by strain gaging ( $E_t \approx 13$  GPa and  $E_c \approx 25$  GPa). The reason for this discrepancy has not been explored yet, but is believed to be due to the fact that elastic modulus estimated by the impulse excitation technique involved a flexural mode of vibration, a combination of *both* tension and compression displacements. This may require a modification of the fundamental flexural-resonance equation in the impulse excitation method if it is used for TBCs that exhibit a difference in elastic modulus between tension and compression. Note that the impulse excitation technique is used primarily for isotropic, homogeneous materials. Elastic modulus of hot-pressed 10 mol% YSZ was found to be  $E = 219$  GPa by the impulse excitation technique (ref. 42).

**Poisson's ratio.**—Figure 13 shows both longitudinal and transverse strains of cylindrical compression test specimens as sprayed and annealed at  $1316^\circ\text{C}$  for 500 h in air, determined by strain gaging. Despite the appreciable nonlinearity in stress-strain curves of the as-sprayed test specimen, Poisson's ratio, which is defined as  $\nu = |\epsilon_2/\epsilon_1|$  (see the figure) for each pair of loading curves, was very low but relatively consistent with  $\nu = 0.04$ , regardless of level of applied stress. By contrast, the annealed test specimen exhibited an increased value of Poisson's ratio,  $\nu = 0.2$ , which is close to the Poisson's ratio of many dense brittle materials. This again shows a change in microstructure from a loosely connected to a closely connected network, due to the sintering effect upon high temperature annealing.

### Directionality

TBCs were fabricated via the plasma-spray process so that anisotropy might be expected because of the prevailing open, splat microstructure preferably aligned perpendicular with respect to the plasma-spray direction. The effect of such anisotropy, as described in the Experimental Techniques section, was determined for as-sprayed TBCs through mode I fracture toughness and Knoop microhardness testing. The results are summarized in table II.

TABLE II.—FRACTURE TOUGHNESS AND KNOOP MICROHARDNESS WITH RESPECT TO MATERIAL DIRECTION FOR PLASMA-SPRAYED ZrO<sub>2</sub>-8 wt% Y<sub>2</sub>O<sub>3</sub> THERMAL BARRIER COATINGS AT AMBIENT TEMPERATURE

Type of testing	Direction or surface <sup>a</sup>	Method <sup>b</sup>	Number of tests	Average values <sup>c</sup>
Fracture toughness, $K_{Ic}$ , MPa $\sqrt{m}$	1	SEVNB	5	1.15(0.07)
	2	SEVNB	4	1.04(0.11)
	3	DCB	4	1.04(0.05)
		<b>Overall average</b>		<b>1.08(0.06)</b>
Microhardness, <sup>d</sup> $H$ , GPa	0°, side	Knoop	5	3.25(0.32)
	90°, side	Knoop	5	3.19(0.86)
	0°, top	Knoop	5	3.31(0.55)
	90°, top	Knoop	5	3.68(1.27)
		<b>Overall average</b>		<b>3.36(0.45)</b>

<sup>a</sup>See figure 4.

<sup>b</sup>SEVNB is single edge V-notched beam and DCB, double cantilever beam.

<sup>c</sup>Numbers in parentheses indicate  $\pm 1.0$  standard deviation.

<sup>d</sup>Indentation load of 9.8 N was used.

The values of fracture toughness additionally determined in directions 2 and 3 (see fig. 4(a)) were  $K_{Ic} = 1.04 \pm 0.11$  and  $1.04 \pm 0.05$  MPa  $\sqrt{m}$ , respectively. These values compare well with  $K_{Ic} = 1.15 \pm 0.07$  MPa  $\sqrt{m}$  in direction 1, described in the foregoing Fracture Toughness section. Therefore, fracture toughness yielded an almost consistent value with only a 10 percent variation in three directions, showing an insignificant directionality response. Note that the expected weakest direction (interlaminar, direction 3) yielded a value of fracture toughness similar to the presumably strongest counterpart (direction 1 or 2).

As for Knoop microhardness as a function of material axis (see fig. 4(b)), a particular interest is in the side surface: the value of microhardness ( $H = 3.25 \pm 0.32$  GPa) parallel to the layers (at 0° angle) was not significantly different from that ( $3.19 \pm 0.86$  GPa) perpendicular to the layers (at 90° angle). Furthermore, Knoop microhardness exhibited little difference between 0 and 90° directions in the top surface, resulting in similar values to those in the side surface. This indicates that as-sprayed TBCs exhibited macroscopically “homogenous” in response to microhardness deformation. However, the somewhat significant scatter in hardness—the COV (coefficient of variation) ranges from 10 to 35 percent—should not be neglected. Also, it must be stated that the value of microhardness was found to be dependent on applied indentation load because of the localized densification of TBCs upon indentation: less localized densification would occur with a lower indentation load, resulting in a higher microhardness value, and vice versa (ref. 29). A value of  $H = 2.7$  GPa was reported for as-sprayed ZrO<sub>2</sub>-8 wt% Y<sub>2</sub>O<sub>3</sub> by Knoop indentation with an indent load of 9.8 N (ref. 12).

As already seen, the elastic modulus of the coating material was similar both in uniaxial tension ( $E \approx 13$  GPa) and in transthickness (interlaminar) tension ( $E \approx 16$  GPa) determined by strain gaging, and there was also reasonable agreement between the values in direction 1 ( $E = 36$  GPa) and direction 2 ( $E = 39$  GPa) obtained from the impulse excitation technique.

A conclusion considering the effect of direction on the mechanical properties can be made: despite their unique complicated, loosely connected, open microstructure, the as-sprayed TBCs used in this work could be categorized as homogeneous materials from a perspective of *macroscopic* continuum mechanics.

## Concluding Remarks

Mechanical properties of free-standing as-sprayed ZrO<sub>2</sub>-8 wt% Y<sub>2</sub>O<sub>3</sub> thermal barrier coatings were described and summarized in this report. The properties examined were strength, fracture toughness, fatigue, constitutive relation, elastic modulus, Poisson’s ratio, and directionality. The loosely connected, open microstructure of the TBCs resulted in unique responses to mechanical loading, so many mechanical

properties and responses of TBCs were unique and different from those of dense polycrystalline ceramics. From the continuum mechanics point of view, directionality of as-sprayed TBCs was found to be macroscopically negligible through the determinations of fracture toughness, Knoop microhardness, and elastic modulus with respect to material axis.

All mechanical properties of the coating materials determined in this work are summarized in the table below. Whether the mechanical properties examined in this study could be applied to thin TBCs as well could only be answered in confidence after thin TBCs are evaluated for these properties. However, some properties may not be able to be measured, as special techniques would be required to determine these properties for thin-coat configurations. As an example of the complexity involved in the testing of thin films, the reader is referred to Muhlstein, Christopher L.; and Brown, Stuart B., eds.: Mechanical Properties of Structural Films. ASTM STP 1413, ASTM, West Conshohocken, PA, 2001. Thus, some properties may not be able to be determined for thin-coat configurations.

Properties	Experimental procedure <sup>a</sup>			Values <sup>b</sup>
	Test method <sup>c</sup>	Test standard	Temperature, °C	
Strength, $\sigma_f$ , MPa	Uniaxial tension	ASTM C 1273	25	15(3)
	Transthickness tension	ASTM C 1468	↓	11(1)
	Uniaxial compression	ASTM C 1424	↓	300(77)
	Uniaxial (four-point) flexure	ASTM C 1161	↓	33(7)
	Biaxial flexure	-----	↓	40(4)
Fracture toughness, <sup>e</sup> MPa $\sqrt{m}$ $K_{Ic}$	SEVNB (symmetric), direction 1	ASTM C 1421 <sup>d</sup>	25 800 1316	1.15 (0.07) 1.03(0.07) 0.98(0.13)
	$K_{IIc}$	-----	25 1316	0.73(0.10) 0.65(0.04)
	$K_{Ic}$	SEVNB, direction 2 DCB, direction 3	ASTM C 1421 <sup>d</sup>	25 25
			25 25	1.04(0.11) 1.04(0.05)
Fatigue (slow crack growth)	Cyclic fatigue (cyclic stress) in tension	ASTM C 1361	25	$n > 100$
	Dynamic fatigue (constant stress rate) in flexure	ASTM C 1465	800	$n > 100$
Elastic modulus, $E$ , GPa	Uniaxial tension (s.g.)	-----	25	13
	Transthickness tension (s.g.)	-----	↓	16
	Compression (s.g.)	-----	↓	25
	Impulse excitation <sup>e</sup>			
	Direction 1	ASTM C 1259		36(2)
	Direction 2	ASTM C 1259		39(2)
	Uniaxial flexure			
	Tension side (s.g.)	-----	↓	24
Poisson's ratio	Compression side (s.g.)	-----	↓	30
	Biaxial flexure (in tension) (s.g.)	-----	↓	44
	Compression		25	0.04
Knoop microhardness, <sup>c</sup> $H$ , GPa	Side surface, 0°	ASTM C 1326	25	3.3(0.3)
	Side surface, 90°	↓	↓	3.2(0.9)
	Top surface, 0°	↓	↓	3.3(0.6)
	Top surface, 90°	↓	↓	3.7(1.3)

<sup>a</sup>All tests conducted in air.

<sup>b</sup>The numbers in parentheses indicate  $\pm 1.0$  standard deviation.

<sup>c</sup>SEVNB is single edge V-notched beam, DCB is double cantilever beam, and s.g. is strain gage.

<sup>d</sup>Test method using SEVNB is not specified in ASTM C 1421, but is followed in compliance with test standard.

<sup>e</sup>See figure 4 for testing locations on specimen.

## References

1. Miller, R.A.: Current Status of Thermal Barrier Coatings—An Overview. *Surf. Coat. Tech.*, vol. 30, no. 1, 1987, pp. 1–11.
2. Miller, R.A.: Thermal Barrier Coatings for Aircraft Engines—History and Directions. Thermal Barrier Coating Workshop, NASA CP-3312, 1996, pp. 17–34.
3. Yonushonis, T.M.: Thick Thermal Barrier Coatings for Diesel Components; Final Report. NASA CR-187111, 1991.
4. Firestone, R.F., et al.: Creep of Plasma-Sprayed  $\text{ZrO}_2$  Thermal-Barrier Coatings. *Ceram. Eng. Sci. Proc.*, vol. 3, nos. 9–10, 1982, pp. 758–771.
5. Eaton, H.E.; and Novak, R.C.: Sintering Studies of Plasma-Sprayed Zirconia. *Surf. Coat. Tech.*, vol. 32, 1987, nos. 1–4.
6. Brink, R.C.: Material Property Evaluation of Thick Thermal Barrier Coating Systems. *J. Eng. Gas Turbines Power*, vol. 111, 1989, pp. 570–577.
7. Cruse, T.A.; Johnsen, B.P.; and Nagy, A.: Mechanical Properties Testing and Results for Thermal Barrier Coatings. *J. Thermal Spray Technol.*, vol. 6, no. 1, 1997, pp. 57–66.
8. Zhu, D.M.; and Miller, R.A.: Sintering and Creep Behavior of Plasma-Sprayed Zirconia- and Hafnia-Based Thermal Barrier Coatings. *Surf. Coat. Tech.*, vol. 108, nos. 1–3, 1998, pp. 114–120.
9. Berndt, C.C., et al.: Influence of Plasma Spray Parameters on Mechanical Properties of Yttria Stabilized Zirconia Coatings. I: Four Point Bend Test. *Mater. Sci. Eng.*, vol. A284, nos. 1–2, 2000, pp. 29–40.
10. Rybicki, E.F., et al.: In Situ Evaluations of Young's Modulus and Poisson's Ratio Using a Cantilever Beam Specimen. *Advances in Thermal Spray Science and Technology, Proceedings of the 8th National Thermal Spray Conference*, C.C. Berndt and S. Sampath, ASM International, Materials Park, OH, 1995, pp. 409–414.
11. Johnson, C.A., et al.: A Method for Measuring Non-Linear Elastic Properties of Thermal Barrier Coatings. *Advances in Thermal Spray Science and Technology, Proceedings of the 8th National Thermal Spray Conference*, C.C. Berndt and S. Sampath, ASM International, Materials Park, OH, 1995, pp. 415–420.
12. Leigh, S.H.; Lin, C.K.; and Berndt, C.C.: Elastic Response of Thermal Spray Deposits Under Indentation Tests. *J. Am. Ceram. Soc.*, vol. 80, no. 8, 1997, pp. 2093–2099.
13. Rejda, E.F.; Socie, D.F.; and Itoh, T.: Deformation Behavior of Plasma-Sprayed Thick Thermal Barrier Coatings. *Surf. Coat. Tech.*, vol. 113, no. 3, 1999, pp. 218–226.
14. Trice, R.W.; Prine, D.W.; and Faber, K.T.: Deformation Mechanisms in Compression-Loaded, Stand-Alone Plasma-Sprayed Alumina Coatings. *J. Am. Ceram. Soc.*, vol. 83, no. 12, 2000, pp. 3057–3064.
15. Cruse, T.A.; Stewart, S.E.; and Ortiz, M.: Thermal Barrier Coating Life Prediction Model Development. *J. Eng. Gas Turbines Power*, vol. 110, no. 4, 1988, pp. 610–616.
16. Wesling, K.F.; Socie, D.F.; and Beardsley, B.: Fatigue of Thick Thermal Barrier Coatings. *J. Am. Ceram. Soc.*, vol. 77, no. 7, 1994, pp. 1863–1868.
17. Johnsen, B.P., et al.: Compressive Fatigue of a Plasma-Sprayed  $\text{ZrO}_2$ -8wt%- $\text{Y}_2\text{O}_3$  and  $\text{ZrO}_2$ -10wt%-Nicalcoy TTBC. *J. Eng. Mater. Technol. Trans. ASME*, vol. 117, no. 3, 1995, pp. 305–310.
18. Shaw, L.L., et al.: Measurements of the Interfacial Fracture Energy of Thermal Barrier Coatings. *Scr. Mater.*, vol. 39, no. 10, 1998, pp. 1427–1434.
19. Callus, P.J.; and Berndt, C.C.: Relationships Between the Mode II Fracture Toughness and Microstructure of Thermal Spray Coatings. *Surf. Coat. Tech.*, vol. 114, nos. 2–3, 1999, pp. 114–128.
20. Thurn, G., et al.: Toughness Anisotropy and Damage Behavior of Plasma Sprayed  $\text{ZrO}_2$  Thermal Barrier Coatings. *Surf. Coat. Tech.*, vol. 123, nos. 2–3, 2000, pp. 147–158.

21. Zhou, Y.C., et al.: Fracture Characteristics of Thermal Barrier Coatings After Tensile and Bending Tests. *Surf. Coat. Tech.*, vol. 157, nos. 2–3, 2002, pp. 118–127.
22. Evans, A.G., et al.: Mechanisms Controlling the Durability of Thermal Barrier Coatings. *Prog. Mater. Sci.*, vol. 46, no. 5, 2001, pp. 505–553.
23. Steinbrech, R.W.: Thermomechanical Behavior of Plasma Sprayed Thermal Barrier Coatings. *Ceram. Eng. Sci. Proc.*, vol. 23, no. 4, 2002, pp. 397–408.
24. Choi, S.R.: High-Temperature Slow Crack Growth, Fracture Toughness and Room-Temperature Deformation Behavior of Plasma-Sprayed  $\text{ZrO}_2$ -8wt%  $\text{Y}_2\text{O}_3$ . *Ceram. Eng. Sci. Proc.*, vol. 19, no. 4, 1998, pp. 293–301.
25. Choi, S.R.; Zhu, D.; and Miller, R.A.: Flexural and Compressive Strengths and Room-Temperature Creep/Relaxation Properties of Plasma-Sprayed  $\text{ZrO}_2$ -8wt%  $\text{Y}_2\text{O}_3$ . *Ceram. Eng. Sci. Proc.*, vol. 20, issue 3, 1999, pp. 365–372.
26. Choi, S.R.; and Zhu, D.; and Miller, R.A.: Deformation and Strength Behavior of Plasma-Sprayed  $\text{ZrO}_2$ -8wt%  $\text{Y}_2\text{O}_3$  Thermal Barrier Coatings in Biaxial Flexure and Trans-Thickness Tension. *Ceram., Eng. Sci. Proc.*, vol. 21, no. 4, 2000, pp. 653–661.
27. Choi, S.R.; Zhu, D.M.; and Miller, R.A.: Deformation and Tensile Cyclic Fatigue of Plasma-Sprayed  $\text{ZrO}_2$ -8wt%  $\text{Y}_2\text{O}_3$  Thermal Barrier Coatings. *Ceram. Eng. Sci. Proc.*, vol. 22, no. 4, 2001, pp. 427–434, 2001.
28. Choi, Sung R., Zhu, Dongming, and Miller, Robert A.: Mode I, Mode II, and Mixed-Mode Fracture of Plasma-Sprayed Thermal Barrier Coatings at Ambient and Elevated Temperatures. NASA/TM—2003-212185, 2003.
29. Choi, Sung R.; Zhu, Dong-Ming, and Miller, Robert A.: Effect of Sintering on Mechanical and Physical Properties of Plasma-Sprayed Thermal Barrier Coatings. NASA/TM—2004-212625, 2004.
30. Zhu, D.M.; and Miller, R.A.: Thermal Conductivity and Elastic Modulus Evolution of Thermal Barrier Coatings Under High Heat Flux Conditions. *J. Therm. Spray Tech.*, vol. 9, no. 2, 2000, pp. 175–180.
31. Test Method for Tensile Strength of Monolithic Advanced Ceramics at Ambient Temperatures. Annual Book of ASTM Standards 2004, ASTM Designation: C 1273–95a(2000), section 15, vol. 15.01, ASTM, West Conshohocken, PA, 2004.
32. Test Method for Transthickness Tensile Strength of Continuous Fiber-Reinforced Advanced Ceramics at Ambient Temperature. Annual Book of ASTM Standards 2004, ASTM Designation: C 1468–00, section 15, vol. 15.01, ASTM, West Conshohocken, PA, 2004.
33. Test Method for Monotonic Compressive Strength of Advanced Ceramics at Ambient Temperature. Annual Book of ASTM Standards 2004, ASTM Designation: C 1424–99, section 15, vol. 15.01, ASTM, West Conshohocken, PA, 2004.
34. Test Method for Flexural Strength of Advanced Ceramics at Ambient Temperature. Annual Book of ASTM Standards 2004, ASTM Designation: C 1161–02c, section 15, vol. 15.01, ASTM, West Conshohocken, PA, 2004.
35. a. Kübler, J.: Fracture Toughness of Ceramics Using the SEVNB Method: Preliminary Results. *Cer. Eng. Sci. Proc.*, vol. 18, issue 4, 1997.  
b. Quinn, G.; Kübler, J.; and Gettings, J.: Fracture Toughness of Advanced Ceramics by the Surface Crack in Flexure (SCF) Method: A VAMAS Round Robin. VAMAS Report No. 17, NIST, Gaithersburg, MD, 1994.
36. Test Methods for Determination of Fracture Toughness of Advanced Ceramics at Ambient Temperature. Annual Book of ASTM Standards 2004, ASTM Designation: C 1421–01b, section 15, vol. 15.01, ASTM, West Conshohocken, PA, 2004.
37. Test Method for Determination of Slow Crack Growth Parameters of Advanced Ceramics by Constant Stress-Rate Flexural Testing at Ambient Temperature. Annual Book of ASTM Standards 2004, ASTM Designation: C 1368–01, section 15, vol. 15.01, ASTM, West Conshohocken, PA, 2004.

38. Test Method for Determination of Slow Crack Growth Parameters of Advanced Ceramics by Constant Stress-Rate Flexural Testing at Elevated Temperatures. Annual Book of ASTM Standards 2004, ASTM Designation: C 1465–00, section 15, vol. 15.01, ASTM, West Conshohocken, PA, 2004.
39. Test Method for Dynamic Young's Modulus, Shear Modulus, and Poisson's Ratio for Advanced Ceramics by Impulse Excitation of Vibration. Annual Book of ASTM Standards 2004, ASTM Designation: C 1259–01, section 15, vol. 15.01, ASTM, West Conshohocken, PA, 2004.
40. Murakami, Y., ed.: Stress Intensity Factors Handbook. Pergamon, New York, NY, 1987.
41. Test Method for Knoop Indentation Hardness of Advanced Ceramics. Annual Book of ASTM Standards 2004, ASTM Designation: C 1326–03, section 15, vol. 15.01, ASTM, West Conshohocken, PA, 2004.
42. a. Choi, Sung R.; and Bansal, Narottam P.: Processing and Mechanical Properties of Various Zirconia/Alumina Composites for Fuel Cell Applications. NASA/TM—2002-211580, 2002.  
b. Choi, S.R.; and Bansal, N.P.: Strength and Fracture Toughness of Zirconia/Alumina Composite for Solid Oxide Fuel Cells. Cer. Eng. Sci. Proc., vol. 23, issue 3, 2002, pp. 741–750.
43. Shetty, D.K.; Rosenfield, A.R.; and Duckworth, W.H.: Mixed-Mode Fracture of Ceramics in Diametral Compression. J. Am. Ceram. Soc., vol. 69, no. 6, 1986, pp. 437–443.
44. Tikare, V.; and Choi, S.R.: Combined Mode-I and Mode-II Fracture of Monolithic Ceramics. J. Am. Ceram. Soc., vol. 76, no. 9, 1993, pp. 2265–2272.
45. Tikare, V.; and Choi, S.R.: Combined Mode I–Mode II Fracture of 12-mol%-Ceria-Doped Tetragonal Zirconia Polycrystalline Ceramic. J. Am. Ceram. Soc., vol. 80, no. 6, 1997, pp. 1624–1626.
46. Lange, F.F.: Transformation Toughening. 3. Experimental-Observations in the  $\text{ZrO}_2\text{-Y}_2\text{O}_3$  System. J. Mat. Sci., vol. 17, no. 1, 1982, pp. 240–246.
47. Shimada, M., et al.: Temperature-Dependence of Young Modulus and Internal-Friction in Alumina, Silicon-Nitride, and Partially Stabilized Zirconia Ceramics. J. Am. Cer. Soc., vol. 67, no. 2, 1984, pp. C23–C24.
48. Wesling, K.F.; Socie, D.F.; and Beardsley, B.: Fatigue of Thick Thermal Barrier Coatings. J. Am. Cer. Soc., vol. 77, no. 7, 1994, pp. 1863–1868.

REPORT DOCUMENTATION PAGE			Form Approved OMB No. 0704-0188	
Public reporting burden for this collection of information is estimated to average 1 hour per response, including the time for reviewing instructions, searching existing data sources, gathering and maintaining the data needed, and completing and reviewing the collection of information. Send comments regarding this burden estimate or any other aspect of this collection of information, including suggestions for reducing this burden, to Washington Headquarters Services, Directorate for Information Operations and Reports, 1215 Jefferson Davis Highway, Suite 1204, Arlington, VA 22202-4302, and to the Office of Management and Budget, Paperwork Reduction Project (0704-0188), Washington, DC 20503.				
1. AGENCY USE ONLY (Leave blank)		2. REPORT DATE November 2004		3. REPORT TYPE AND DATES COVERED Technical Memorandum
4. TITLE AND SUBTITLE  Mechanical Properties of Plasma-Sprayed ZrO <sub>2</sub> -8 wt% Y <sub>2</sub> O <sub>3</sub> Thermal Barrier Coatings			5. FUNDING NUMBERS  WBS-22-714-04-05	
6. AUTHOR(S)  Sung R. Choi, Dongming Zhu, and Robert A. Miller				
7. PERFORMING ORGANIZATION NAME(S) AND ADDRESS(ES)  National Aeronautics and Space Administration John H. Glenn Research Center at Lewis Field Cleveland, Ohio 44135-3191			8. PERFORMING ORGANIZATION REPORT NUMBER  E-14724	
9. SPONSORING/MONITORING AGENCY NAME(S) AND ADDRESS(ES)  National Aeronautics and Space Administration Washington, DC 20546-0001			10. SPONSORING/MONITORING AGENCY REPORT NUMBER  NASA TM-2004-213216	
11. SUPPLEMENTARY NOTES  Sung R. Choi, Ohio Aerospace Institute, Brook Park, Ohio 44142; Dongming Zhu, U.S. Army Research Laboratory, NASA Glenn Research Center; and Robert A. Miller, Glenn Research Center. Responsible person, Sung R. Choi, organization code 5920, 216-433-8366.				
12a. DISTRIBUTION/AVAILABILITY STATEMENT  Unclassified - Unlimited Subject Category: 07  Available electronically at <a href="http://gltrs.grc.nasa.gov">http://gltrs.grc.nasa.gov</a> This publication is available from the NASA Center for AeroSpace Information, 301-621-0390.			12b. DISTRIBUTION CODE	
13. ABSTRACT (Maximum 200 words)  Mechanical behavior of free standing, plasma-sprayed ZrO <sub>2</sub> -8 wt% Y <sub>2</sub> O <sub>3</sub> thermal barrier coatings, including strength, fracture toughness, fatigue, constitutive relation, elastic modulus, and directionality, has been determined under various loading-specimen configurations. This report presents and describes a summary of mechanical properties of the plasma-sprayed coating material to provide them as a design database.				
14. SUBJECT TERMS  Thermal barrier coatings; Mechanical properties; Strength; Fracture toughness; Fatigue; Deformation; Elastic modulus; Directionality; Plasma-sprayed ZrO <sub>2</sub> -8 wt% Y <sub>2</sub> O <sub>3</sub>			15. NUMBER OF PAGES 24	
			16. PRICE CODE	
17. SECURITY CLASSIFICATION OF REPORT  Unclassified	18. SECURITY CLASSIFICATION OF THIS PAGE  Unclassified	19. SECURITY CLASSIFICATION OF ABSTRACT  Unclassified	20. LIMITATION OF ABSTRACT	





